

DC/DC Converter Design for Supercapacitor and Battery Power Management in Hybrid Vehicle Applications—Polynomial Control Strategy

Mamadou Bailo Camara, Hamid Gualous, Frederic Gustin,
Alain Berthon, *Member, IEEE*, and Brayima Dakyo, *Member, IEEE*

Abstract—This paper presents supercapacitor (SCAP) and battery modeling with an original energy management strategy in a hybrid storage technology. The studied dc power supply is composed of SCAPs and batteries. SCAPs are dimensioned for peak power requirement, and batteries provide the power in steady state. A bidirectional dc/dc converter is used between SCAPs and the dc bus. Batteries are directly connected to the dc bus. The originality of this study is focused on SCAP behavior modeling and energy management strategy. The proposed strategy is based on a polynomial (RST) controller. For reasons of cost and existing components (not optimized) such as batteries and semiconductors, the experimental test benches are designed in reduced scale. The characterized packs of SCAPs include two modules of ten cells in series for each one and present a maximum voltage of 27 V. The proposed strategy is implemented on a PIC18F4431 microcontroller for two dc/dc converter topology controls. Experimental and simulation results obtained from the polynomial control strategy are presented, analyzed, and compared with that of classical proportional–integral control.

Index Terms—Batteries, buck–boost converter, dynamic control, electric hybrid vehicle (HEV), energy management, energy storage, polynomial control strategy, power management, supercapacitors.

I. INTRODUCTION

MANY research works are undertaken on technologies of future vehicles. Battery power request in transient state decreases its life span. To solve this problem of battery and supercapacitor (SCAP) hybridization, there must be good energy management between these devices which enables the reduction of the battery size and improves its life span. The

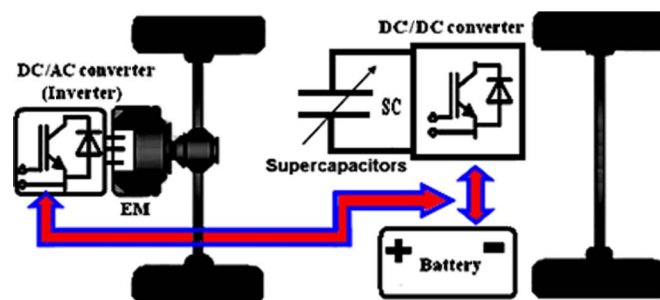


Fig. 1. SCAP and battery HEV topology.

battery and SCAP energy coupling improves the autonomy and performance of the vehicle. For autonomy problems, the traction battery used until now cannot satisfy the energy needs of future vehicles. An electric hybrid vehicle (HEV) is a vehicle that combines, in addition to its main energy source (oil and gas), reverse energy storage devices like flywheels, SCAPs, and batteries. These technologies which associate SCAPs and batteries (Fig. 1) are very promising in short and medium terms due to the SCAPs' high dynamic performances and their life span of about ten years longer than that of a battery. The SCAPs have power density from 10 to 100 times larger than that of a battery with an energy density that is much smaller. Moreover, these high-power storage devices present less risk of pollution than batteries. The hybrid vehicle associates the advantages of thermal vehicles (autonomy and flexibility) and electric vehicles (no pollution), but it is not simple to combine these models, because the devices must be optimized. The main contribution of this paper presents two aspects.

The first is based on SCAP behavior modeling with an original method for experimental parameter identification.

The second aspect is focused on a novel strategy of embedded energy management using RST controllers.

To validate the proposed method, a SCAP module and two dc/dc converter topologies are designed at reduced scale. This solution is due to the reason of cost and existing components, such as the batteries and the semiconductors. These converters are controlled by a PIC18F4431 microcontroller. The experimental data acquisition system is monitored by using the National Instruments Labview software. For hybrid system simulations, the SABER software package is used.

Manuscript received January 26, 2009; revised June 1, 2009. First published June 16, 2009; current version published January 13, 2010.

M. B. Camara and B. Dakyo are with the Groupe de Recherche en Electrotechnique et Automatique du Havre Laboratory, The University of Le Havre, 76600 Le Havre, France (e-mail: camaram@univ-lehavre.fr; brayima.dakyo@univ-lehavre.fr).

H. Gualous is with the Franche-Comté Electronique Mécanique Thermique et Optique—Sciences et Technologies Institute, University of Franche-Comté, 90016 Belfort, France (e-mail: hamid.gualous@univ-fcomte.fr).

F. Gustin and A. Berthon are with the Franche-Comté Electronique Mécanique Thermique et Optique—Sciences et Technologies Institute and the Institut Universitaire de Technologie de Belfort–Montbéliard, University of Franche-Comté, 90016 Belfort, France (e-mail: Frederic.gustin@univ-fcomte.fr; alain.berthon@univ-fcomte.fr).

Color versions of one or more of the figures in this paper are available online at <http://ieeexplore.ieee.org>.

Digital Object Identifier 10.1109/TIE.2009.2025283

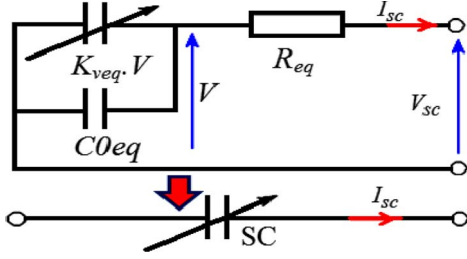
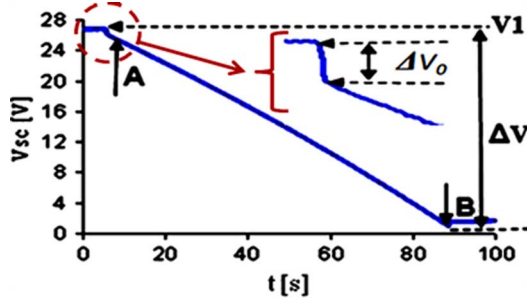


Fig. 2. Electrical model of SCAPs.

Fig. 3. SCAP module experimental voltage for $I_{sc} = 80$ A.

II. BATTERY AND SCAP MODELING

A. SCAP Modeling and Characterization

To use SCAPs as energy storage devices [1] in HEV, it is necessary to associate several cells in series to obtain a high voltage level since each cell voltage is 2.7 V. The SCAP model used includes an internal resistance R_{eq} and an equivalent capacitance including two components. The main component $K_{veq} \cdot V$ varies linearly with the SCAP module voltage, and the second component C_{0eq} is a constant capacitor [2]. The studied electrical behavior model of the SCAP module is shown in Fig. 2. This model describes the immediate behavior of the SCAP in the time range of seconds in response to a charge or discharge action.

To estimate the SCAP module parameters, a module including ten cells of the Maxwell Technology SCAPs (BOOSTCAP) is used. This module presents a maximum voltage of 27 V. The parameter estimation is based on the analysis of the SCAP module experimental discharge at constant current. The experimental voltage measured during the SCAP module discharge at 80 A is shown in Fig. 3. The early discharge of the module is characterized by a voltage drop (ΔV_0 in Fig. 3) in internal resistance R_{eq} , and this resistance can be estimated by using

$$R_{eq} = R_{sc} + R_{con} = \frac{\Delta V_0}{I_{sc}}. \quad (1)$$

The assumed linear behavior of the differential capacitance $C_{0eq} + K_{veq} \cdot V$ enables one to estimate the β_0 coefficient from an approximation of the segment AB (Fig. 4). A and B have the following coordinates $A(t_1, V_{sc}(t_1))$ and $B(t_2, V_{sc}(t_2))$, respectively. The resulting equation from these conditions is presented as

$$\beta_0 \approx \left| \frac{V_{sc}(t_1) - V_{sc}(t_2)}{t_2 - t_1} \right| \approx 0.3115. \quad (2)$$

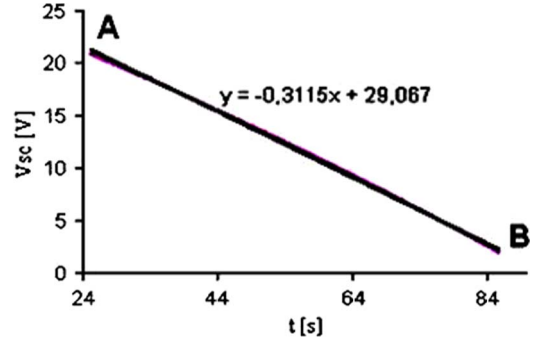
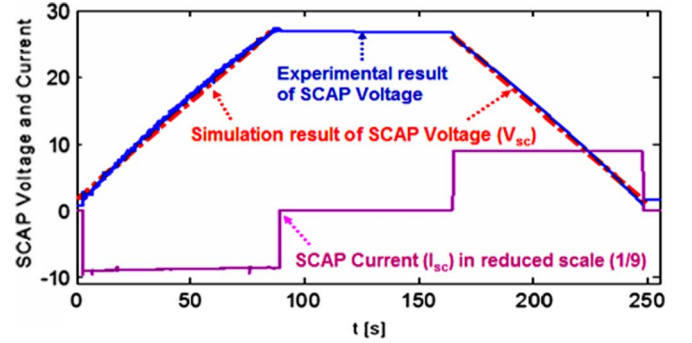
Fig. 4. AB segment approximation for $I_{sc} = 80$ A with $x = t$.

TABLE I
SCAP EXPERIMENTAL PARAMETERS

NAME	Symbol	Value	Unit
Cells number	N_s	10	-
Cells resistance	R_{sc}	4.28	m Ω
Connectors resistance	R_{con}	4.47	m Ω
Constant capacitor	C_{0eq}	256	F
Specific capacity	K_{veq}	0.204	F/V

Fig. 5. SCAP charge and discharge current (-80 A, 0, and 80 A) and voltage.

The module capacitances K_{veq} and C_{0eq} resulting from experimental curve analysis can be estimated by (3), where Δt presents the SCAP module discharge time in seconds. In the following, V_1 and ΔV present the SCAP module initial voltage and module voltage variation between V_1 and the final voltage (minimum value), respectively:

$$\begin{cases} K_{veq} = \left(\frac{1}{\beta_0} - \frac{\Delta t}{\Delta V} \right) \cdot \frac{I_{sc}}{2 \cdot V_1 - 0.5 \cdot \Delta V} \\ C_{0eq} = \left(\frac{1}{\beta_0} - \left(\frac{1}{\beta_0} - \frac{\Delta t}{\Delta V} \right) \cdot \frac{2 \cdot V_1}{2 \cdot V_1 - 0.5 \cdot \Delta V} \right) \cdot I_{sc}. \end{cases} \quad (3)$$

The experimental parameters for ten cells of the BOOSTCAP2600F module obtained from (1) and (3) are presented in Table I. To validate the model, the SCAP module was charged to maximum voltage (27 V) and discharged with constant currents of -80 and 80 A, respectively, as shown in Fig. 5. The comparison of the simulation and experimental results obtained from these conditions is shown in Fig. 5. This model gives the SCAP behavior during the charge and discharge, but it is limited, because it does not describe the SCAP behavior before and after the charge and discharge, i.e., for $I_{sc} = 0$. This aspect (self-discharge) is studied in [3]. The proposed SCAP model in this paper is satisfactory for HEV applications, and it will be used for the global system simulations.

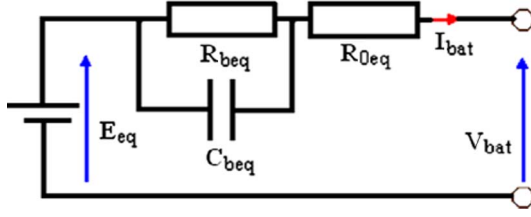


Fig. 6. Dynamic model of the battery.

B. Battery Modeling

Generally, in HEV applications, the lead-acid technology is less used compared with technologies of nickel–metal hydride (Ni-MH) and lithium ion. However, for the reason of cost, the lead-acid battery will be used in this test bench to validate the embedded energy management strategy. The existing models in literature [4]–[8] for lead-acid technology are generally complex to implement because of the several parameters to be estimated. In these models, the temperature is a very important parameter which has a great influence on the battery operation. This parameter affects the electrochemical system behavior and the HEV performance. The model used (Fig. 6) includes a constant source E_{eq} (EMF) with internal impedance Z_{bat} which characterizes the battery. Equation (4) is used for the battery capacity estimation in the simulation model, where θ is the electrolyte temperature in degrees Celsius, I_n is the battery rated current, and C_0 , K_c , ε , θ_f , and δ are the constant parameters to be identified [4], [7]. The battery module *SOC* and depth of charge (*DOC*) can be estimated by using (5) and (6), respectively, where *SOC*₀ defines the initial state of charge, and this value is between zero and one

$$C(I, \theta) = \frac{K_c \cdot C_0 \cdot \left(1 - \frac{\theta}{\theta_f}\right)^\varepsilon}{1 + (K_c - 1) \cdot \left(\left|\frac{I}{I_n}\right|\right)^\delta}. \quad (4)$$

The physical meanings of *SOC* and *DOC* are quite simple. The first one gives information on the battery energy stored as compared with maximum energy, which can be ensured by the battery at a temperature of θ . The second one gives information regarding the battery at full charge as compared with the actual discharge state. The electric charge Q_e extracted from the battery during HEV traction state can be estimated by the following:

$$SOC = SOC_0 - \frac{Q_e}{C(0, \theta)}, \quad Q_e(t) = \int_0^t I_{bat}(t) \cdot dt. \quad (5)$$

In (6), the I_{fil} variable is the battery module discharge average current. This current can be obtained by filtering the battery's supplied current

$$DOC = SOC_0 - \frac{Q_e}{C(I_{fil}, \theta)}, \quad I_{fil} = \frac{I_{bat}}{1 + \tau_b \cdot s}. \quad (6)$$

The assumed equations for R_{0eq} , R_{beq} , τ_b , Z_{bat} , and E_{eq} are defined in (7) and (8), where E_0 , K_e , R_0 , A_0 , and R_{10} are constant for a particular battery. The battery model shown in Fig. 6 has been validated by numerous laboratory tests

TABLE II
BATTERY EXPERIMENTAL PARAMETERS

Cells number	$N_b=27$	
Electrolyte temperature	$\theta=30^\circ\text{C}$	
Parameters referring to the battery capacity	$I_n=96\text{A}$	$C_0=96\text{Ah}$
	$K_c=1.509$	$\theta_f=-40^\circ\text{C}$
	$\varepsilon=1.2274$	$\delta=0.9803$
Parameters referring to the main branch of the electric equivalent	$K_e=0.65442\text{mV}/^\circ\text{C}$	$E_0=2.23\text{V}$
	$R_0=8.4\text{m}\Omega$	$R_{10}=4.35\text{m}\Omega$
	$A_0=-0.152063$	$\tau_b=910\text{s}$

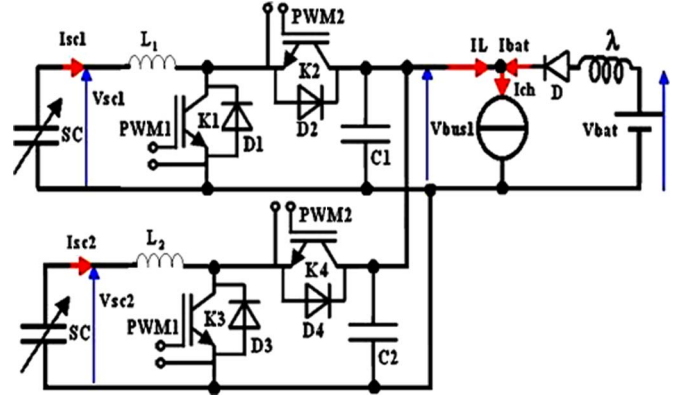


Fig. 7. First topology of the buck–boost converters.

using one test bench. All parameter estimation strategies are described by [4], [7]

$$\begin{cases} R_{0eq} = N_b \cdot R_0 \cdot (1 + A_0 \cdot (1 - SOC)) \\ R_{beq} = -N_b \cdot R_{10} \cdot \ln(DOC) \\ R\tau_b = R_{beq} \cdot C_{beq} \\ Z_{bat} = R_{0eq} + \frac{R_{beq}}{1 + j\omega \cdot \tau_b} \end{cases} \quad (7)$$

$$V_{bat} = N_b \cdot (E_0 - K_e \cdot (273 + \theta)(1 - SOC)) - Z_{bat} \cdot I_{bat}. \quad (8)$$

The battery parameters identified from several experimental tests are shown in Table II.

III. DC/DC CONVERTER MODELING AND CONTROL

The main goal of this paragraph is to establish the dc/dc converter control laws for energy management between the SCAPs and the battery. This study is based on the two buck–boost [9]–[20] converters with parallel topology. The SCAP modules are connected to the dc bus, via two buck–boost converters, which ensure the SCAP charge and discharge. The converter dynamic control strategy is defined by the HEV energy management. The used converter topologies [9]–[11] are shown in Figs. 7 and 8, where the second topology (Fig. 8) allows one to simplify the embedded energy management control strategy and decrease the SCAP current smoothing inductance number.

A. Converter Modeling

To model these converters, the buck and boost [19], [20] converter operating modes must be analyzed. During buck-converter mode, K2 and K4 semiconductors are ON, while

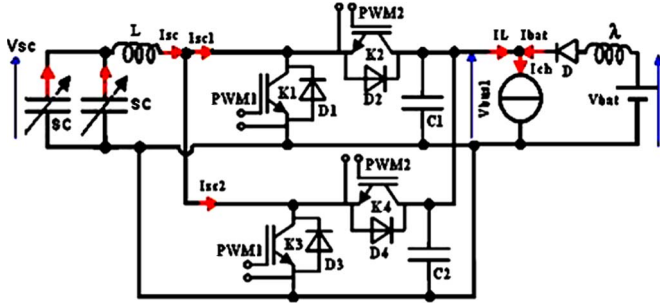


Fig. 8. Second topology of the buck-boost converters.

K1 and K3 are OFF. Contrary to this mode, K1 and K3 are ON, while K2 and K4 went OFF. For this study, the I_{sc1} , I_{sc2} , I_L , I_{bus1} , and I_{bus2} currents are supposed negative during the SCAP energy storage (buck-converter mode), and they are positive during the SCAP discharge (boost-converter mode). The first converter topology (Fig. 7) and the second topology (Fig. 8) average models resulting from the buck/boost converter analysis are given in the following, respectively:

$$\begin{cases} V_{L1} = L_1 \cdot \frac{d}{dt}(I_{sc1}) = k \cdot (V_{sc1} - \alpha \cdot V_{bus1}) \\ V_{L2} = L_2 \cdot \frac{d}{dt}(I_{sc2}) = k \cdot (V_{sc2} - \alpha \cdot V_{bus1}) \\ V_\lambda = \lambda \cdot \frac{d}{dt}(I_{bat}) = V_{bat} - V_{bus1} \end{cases}$$

$$\begin{cases} I_L = I_{bus1} + I_{bus2} \\ I_{ch} = I_{bat} + k \cdot I_L \end{cases} \quad (9)$$

$$\begin{cases} V_L = L \cdot \frac{d}{dt}(I_{sc}) = k \cdot (V_{sc} - \alpha \cdot V_{bus1}) \\ V_{sc1} = V_{sc2} \\ V_\lambda = \lambda \cdot \frac{d}{dt}(I_{bat}) = V_{bat} - V_{bus1} \end{cases}$$

$$\begin{cases} I_L = I_{bus1} + I_{bus2} \\ I_{ch} = I_{bat} + k \cdot I_L. \end{cases} \quad (10)$$

For these analytical models, the k and α variables can have the following values.

- 1) In boost-converter mode, $k = 1$ and $\alpha = 1 - \alpha_1$, where α_1 is the boost-converter duty-cycle average value.
- 2) In buck-converter mode, $k = -1$ and $\alpha = \alpha_2$, where α_2 is the buck-converter duty-cycle average value.

These models have a nonlinear behavior because of crosses between the control variables (α_1 and α_2) and the state variables (I_{sc1} , I_{sc2} , and V_{bus1}), as shown in Fig. 9. The V_{sc1} , V_{sc2} , V_{bus1} , I_{ch} , and V_{bat} variables are likely to disturb the control; they are measured and used in the control law estimation to ensure a dynamic control. This nonlinear behavior is studied in [11].

The first-topology control laws which result from the boost and buck converter modeling are defined by α_1 and α_2 estimated duty cycles, respectively

$$\alpha_1 = 1 - \frac{1}{2} \cdot \frac{(V_{sc1} + V_{sc2}) - (V_{L1} + V_{L2})}{(V_{bat} - V_\lambda)}$$

$$\alpha_2 = \frac{1}{2} \cdot \frac{(V_{L1} + V_{L2}) + (V_{sc1} + V_{sc2})}{V_{bus1}}. \quad (11)$$

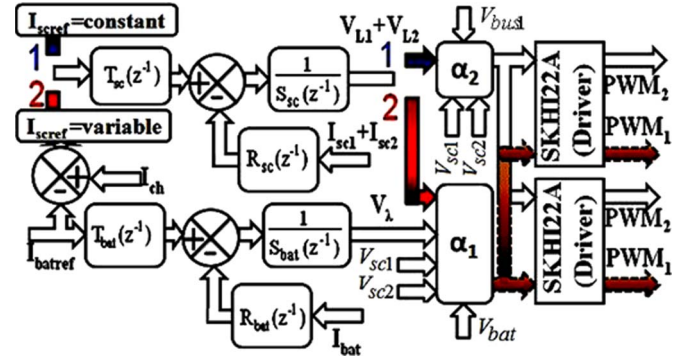


Fig. 9. Implemented polynomial control for buck and boost converters.

The second-topology control strategy can be obtained from the first-topology control strategy by using

$$V_L = \frac{V_{L1} + V_{L2}}{2} \quad V_{sc} = \frac{V_{sc1} + V_{sc2}}{2}. \quad (12)$$

B. Polynomial (RST) Control Strategy

This study is based on the polynomial (RST) dynamic control strategy [21]–[23] of the buck-boost converters for energy management between the battery and SCAPs. The control strategy must be of current type because the dc-bus voltage level is fixed by the battery. The RST controllers give a robust algorithm, with good performances in the case of the following processes:

- 1) with a pure delay;
- 2) whose dynamic characteristics change during operation;
- 3) where the reference should not be exceeded.

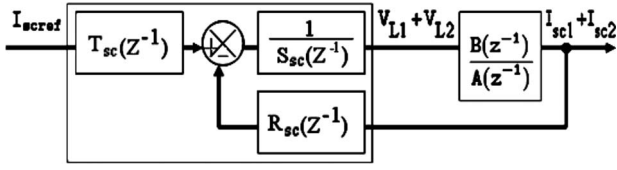
The first-topology control strategy (Fig. 9) presents two distinct phases. The first phase is characterized by the charge of the SCAP with constant current ($I_{scref} = const$). During this phase, the battery current loop is not activated, i.e., only the PWM2 signal is activated (1 is ON and 2 is OFF). In this state, only one RST controller is used.

The second phase is characterized by the discharge of the SCAP with variable current. The SCAP current reference $I_{scref} = I_{scref1} + I_{scref2}$ is obtained starting from energy management between battery and SCAP (13), where η_1 (first boost) and η_2 (second boost) present the two parallel boost-converter theoretical efficiencies (100% for simulations). During this phase, the SCAP and battery current loops with PWM1 control signal are activated (1 is OFF and 2 is ON). In this case, two controllers are used for SCAP and battery current control. The PWM1 and PWM2 signals cannot be activated simultaneously

$$\begin{cases} I_{sc1ref} = \frac{1}{2} \cdot \frac{V_{bus1}}{\eta_1 \cdot V_{sc1}} \cdot (I_{ch} - I_{batref}) \\ I_{sc2ref} = \frac{1}{2} \cdot \frac{V_{bus1}}{\eta_2 \cdot V_{sc2}} \cdot (I_{ch} - I_{batref}) \end{cases}$$

$$I_{scref} = I_{sc1ref} + I_{sc2ref}. \quad (13)$$

For RST parameter estimation, the sampling-process transfer functions obtained from (9) and (10) are presented in (14). The converter control strategy can be simplified if $L_1 = L_2$, and

Fig. 10. r_{0sc} and r_{1sc} estimation for two converter controls.

the general transfer function resulting from this assumption is presented in (15)

$$\begin{cases} G_1(z^{-1}) = \frac{I_{sc1}(z^{-1})}{V_{L1}(z^{-1})} = \frac{T_e}{L_1} \cdot \frac{z^{-1}}{1-z^{-1}} \\ F(z^{-1}) = \frac{I_{bat}(z^{-1})}{V_{\lambda}(z^{-1})} = \frac{T_e}{\lambda} \cdot \frac{z^{-1}}{1-z^{-1}} \end{cases}$$

$$G_2(z^{-1}) = \frac{I_{sc2}(z^{-1})}{V_{L2}(z^{-1})} = \frac{T_e}{L_2} \cdot \frac{z^{-1}}{1-z^{-1}} \quad (14)$$

$$G_1(z^{-1}) = G_2(z^{-1}) = \frac{I_{sc1}(z^{-1}) + I_{sc2}(z^{-1})}{V_{L1}(z^{-1}) + V_{L2}(z^{-1})}. \quad (15)$$

The RST control strategy method consists of identifying $R(z^{-1})$, $S(z^{-1})$, and $T(z^{-1})$ polynomials from an imposed model in closed loop, where $R(z^{-1})$ and $S(z^{-1})$ ensure the role of the regulation and $T(z^{-1})$ ensures the system control. The Diophantine equation [21] gives $R(z^{-1})$ and $S(z^{-1})$ polynomials. The $G_1(z^{-1})$ and $F(z^{-1})$ transfer functions in closed loop are similar; this is why only one method is presented for $R(z^{-1})$, $S(z^{-1})$, and $T(z^{-1})$ polynomial identification by using $G_1(z^{-1})$. The desired polynomial in closed loop is presented in

$$P(z^{-1}) = 1 + p_1 \cdot z^{-1} + p_2 \cdot z^{-2}. \quad (16)$$

This polynomial is of second order, and then, the closed-loop transfer-function characteristic equation must be equal to second order. In other words, the orders of $A(z^{-1})$ and $B(z^{-1})$ are equal to 1, and those of $R(z^{-1})$ and $S(z^{-1})$ must also be equal to 1. The SCAP current-control polynomial must be obtained by using the closed-loop system shown in Fig. 10. In this case, the balancing issue between I_{sc1} and I_{sc2} is not significant when the two SCAP modules are balanced and when the two converters are the same. The $A(z^{-1})$ and $B(z^{-1})$ polynomials for the $G_1(z^{-1})$ transfer function are given in

$$A(z^{-1}) = 1 - z^{-1} \quad B(z^{-1}) = \frac{T_e}{L_1} \cdot z^{-1}. \quad (17)$$

To obtain a minimal static error in HEV energy management with a disturbance rejection, the $R(z^{-1})$ and $S(z^{-1})$ polynomials presented in the following are selected:

$$S(z^{-1}) = 1 - z^{-1} \quad R(z^{-1}) = r_{0sc} + r_{1sc} \cdot z^{-1}. \quad (18)$$

The sampling-process transfer function resulting from the closed-loop system enables one to write

$$F_{cl}(z^{-1}) = \frac{T(z^{-1}) \cdot B(z^{-1})}{A(z^{-1}) \cdot S(z^{-1}) + B(z^{-1}) \cdot R(z^{-1})}. \quad (19)$$

To choose the $T(z^{-1})$ polynomial, two methods are possible.

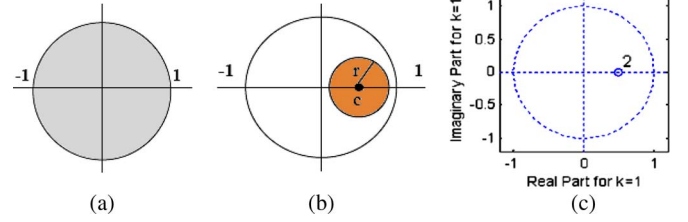


Fig. 11. Robust stability and robust performance analysis.

The first method consists of choosing two different polynomials of $T(z^{-1})$ and $R(z^{-1})$. In this case, the simplest solution is to identify the $T(z^{-1})$ polynomial for a static gain equal to 1. This condition is presented in (20), and the resulting equation from this comparison is given in (21)

$$T(1) \cdot B(1) = A(1) \cdot S(1) + B(1) \cdot R(1) \quad (20)$$

$$T(1) = r_{0sc} + r_{1sc}. \quad (21)$$

The second method [22], [23] consists of choosing $T(z^{-1})$ and $R(z^{-1})$ that are identical to reduce the number of parameters to be identified (22). This last method is described and used in this paper

$$T(z^{-1}) = R(z^{-1}). \quad (22)$$

$R(z^{-1})$ polynomial coefficients are identified, using a simple comparison between the $P(z^{-1})$ desired polynomial and the denominator of the transfer function in closed loop

$$P(z^{-1}) = A(z^{-1}) \cdot S(z^{-1}) + B(z^{-1}) \cdot R(z^{-1}) \quad (23)$$

$$\begin{aligned} r_{0sc} &= (p_1 + 2) \cdot \frac{L_1}{T_e} \\ r_{1sc} &= (p_2 - 1) \cdot \frac{L_1}{T_e}. \end{aligned} \quad (24)$$

The resulting coefficients from this comparison are presented in (24), where the P_1 and P_2 coefficients depend on the dynamic system in closed loop. These coefficients can be obtained by using the following desired polynomial:

$$P(z^{-1}) = (1 - z^{-1} \cdot \exp(-\omega_n \cdot T_e))^2. \quad (25)$$

To ensure a robust stability of the system, the closed-loop poles must be remaining inside the unit circle (discrete-time case) for all the models [Fig. 11(a)]. Concerning the robust performance evaluation, the closed-loop poles must be remaining inside the circle (c, r) , as shown in Fig. 11(b). The obtained poles from this method using (25) are shown in Fig. 11(c). This curve shows that the conditions of stability and robust performance are respected. Equation (26) presents the SCAP current-loop polynomial approximate coefficients, according to L_1 inductance, T_e sampling period, and the bandwidth ($\omega_n \geq \text{Log}(2)/T_e$). To choose the r_{0sc} and r_{1sc} coefficients, inside the bandwidth, a k parameter is introduced as presented in the following expression ($\omega_n = k \cdot \text{Log}(2)/T_e$). This variable is

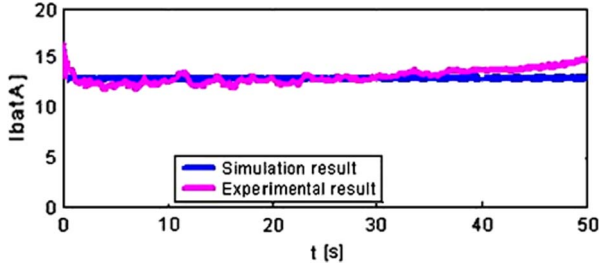


Fig. 12. Battery-current-control result.

selected between 1 and 2, and it gives all possible values of the bandwidth

$$\begin{cases} r_{0sc} = 2 \cdot (1 - \exp(-\omega_n \cdot T_e)) \cdot \frac{L_1}{T_e} \approx 2 \cdot \left(1 - \frac{1}{1 + \omega_n \cdot T_e}\right) \cdot \frac{L_1}{T_e} \\ r_{1sc} = (\exp(-2 \cdot \omega_n \cdot T_e) - 1) \cdot \frac{L_1}{T_e} \approx \left(\frac{1}{1 + 2 \cdot \omega_n \cdot T_e} - 1\right) \cdot \frac{L_1}{T_e} \end{cases} \quad (26)$$

The $G_1(z^{-1})$ and $F(z^{-1})$ discretized processes are similar; in other words, the battery-current-loop polynomial coefficients can be obtained while replacing L_1 by λ as presented in (27). This operation enables one to write the battery-current-control polynomial approximate coefficients

$$\begin{aligned} r_{0bat} &\approx 2 \cdot \left(1 - \frac{1}{1 + \omega_n \cdot T_e}\right) \cdot \frac{\lambda}{T_e} \\ r_{1bat} &\approx \left(\frac{1}{1 + 2 \cdot \omega_n \cdot T_e} - 1\right) \cdot \frac{\lambda}{T_e} \end{aligned} \quad (27)$$

These coefficients are respectively implemented in the PIC18F4431 microcontroller and SABER software for control of the test bench and system simulations in the reduced scale.

C. Second-Topology Simulation and Experimental Results

The boost-converter experimental test is carried out in the following conditions: During the SCAP discharge, the battery current reference (I_{batref}) is fixed at 14 A so that the SCAP modules provide HEV energy request during the transient states. For these tests, the HEV request I_{ch} was fixed at 54 A.

The comparison of the experimental and simulation results of the battery current is shown in Fig. 12. This figure shows that the battery-current-control strategy is satisfactory during 40 s; after that, it becomes insufficient because of the SCAP discharge. In other words, these curves show that the simulation model developed describes correctly the behavior of the experimental system during the first 40 s. After the first 40 s, the difference that appears between the experimental and simulation results can be explained by the fact that only one SCAP module among the two parallel sets has been characterized. This difference can be eliminated by adjusting the SCAP capacitance value or characterizing the two SCAP modules.

Fig. 13 shows the SCAP experimental and simulation voltages during HEV traction states. These results show that the simulation model developed with SABER software is satisfactory for hybrid-vehicle test-bench behavior description.

The dc-bus current ($I_L = 40$ A) shown in Fig. 14 is ensured by two SCAP modules. The first boost converter (K1-D2)

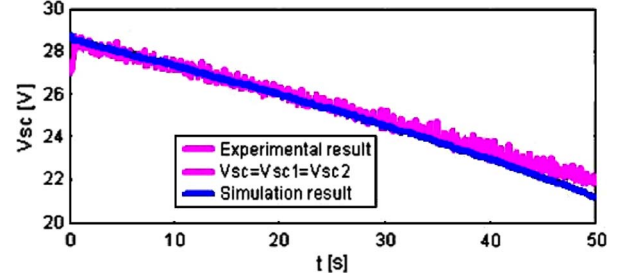


Fig. 13. SCAP module voltages.

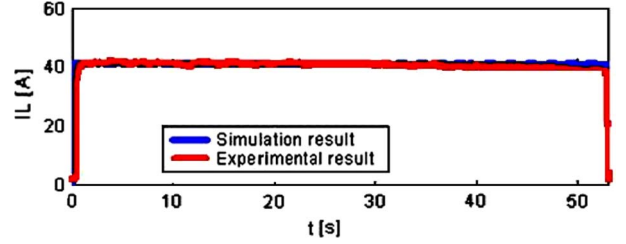


Fig. 14. DC-bus current.

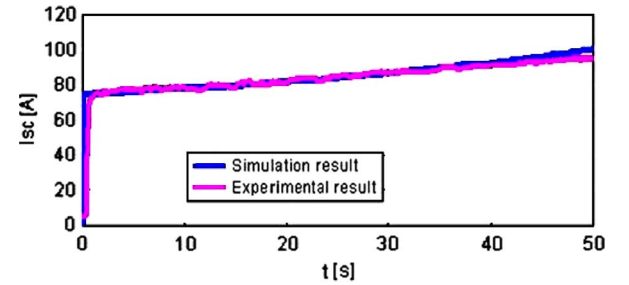


Fig. 15. Supplied current of two SCAP modules.

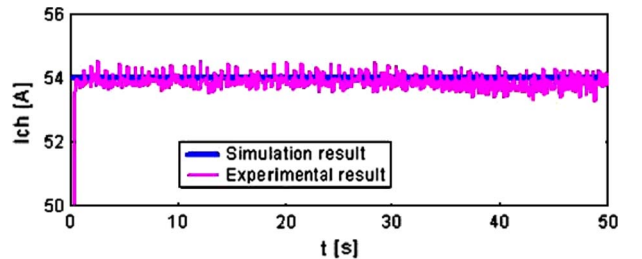


Fig. 16. Active load current.

ensures 50%, and the second (K3-D4) ensures also 50% of the dc-bus current. In other words, the two SCAP modules ensure a current (I_L) of 40 A to HEV, and only 14 A is provided by the battery.

Fig. 15 shows the simulation and experimental results of the two module currents $I_{sc} = I_{sc1} + I_{sc2}$, where I_{sc1} and I_{sc2} are not identical because of the SCAP module dispersion. This figure shows that the control strategy of the SCAP global current I_{sc} is satisfactory during HEV traction state. The simulation and experimentation results of the HEV request current (I_{ch}) are well fitted, and these results are shown in Fig. 16. The experimental tests are carried out with a classical lead-acid battery module that is not entirely charged. This is why one can notice that a difference of about 5 V between the dc-bus voltage V_{bus1} experimental and simulation results (Fig. 17) occurs. This

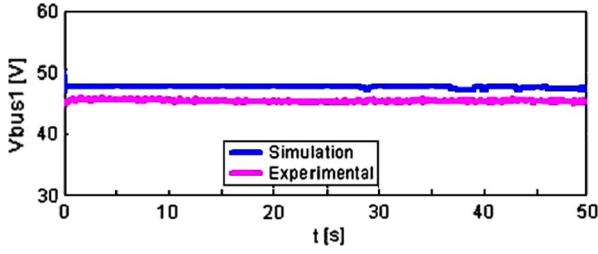


Fig. 17. DC-bus voltage.

TABLE III
TEST-BENCH COMPONENT NOMENCLATURE

Symbol	Name	Value
$L_1=L_2=L$	SCAP currents smoothing inductances	50 μ H
$C_1=C_2=C$	DC-bus voltage filtering capacitors	1500 μ F
λ	Battery current smoothing inductance	25 μ H
$SC_1=SC_2=SC$	SCAP modules	18-27 V

difference is also due to the global system simulation model which is ideal.

IV. DC/DC CONVERTER DESIGN AND EXPERIMENTATION

A. Experimental Setup

For component cost and safety reasons, the experimental test bench is carried out at a reduced scale (1/10). The designed test bench includes two SCAP modules, a battery module, an active load, and a dc/dc converter, which ensures energy management between the battery and SCAP modules. The minimum and maximum voltages of these modules are 13.5 and 27 V, respectively (i.e., ten cells of 2.7 V in series). The battery module, which defines the dc-bus voltage, has a rated voltage of 48 V. DC-bus voltage level must be between 38 and 54 V. An active load is used to define energy request. The whole system is controlled by a PIC18F4431 microcontroller. The test-bench main parameters are presented in Table III.

B. Experimental Test Conditions and Results

Conventionally, the I_{sc1} , I_{sc2} , I_{sc} , I_L , I_{bus1} , and I_{bus2} currents are supposed negative during the SCAP charging, and they are positive during the discharge operation. To show the bidirectional behavior of the converters, the SCAP modules are charged and discharged with constant current (60 A = 30 + 30 A, i.e., 30 A for each module) and variable current (includes between 35 and 52 A for each module), respectively. The charging mode corresponds to SCAP energy storage (I_{sc} negative), and that of the discharge corresponds to the SCAP energy supply to the dc bus (I_{sc} positive). If the modules are discharged more than 75%, the dynamic control becomes insufficient because of the weakened SCAP voltage.

To ensure a comparative study, two bidirectional converter topologies are carried out. For all experimental tests, the minimum and maximum voltages of the modules are fixed at 18 and 27 V, respectively. The HEV current request I_{ch} is fixed

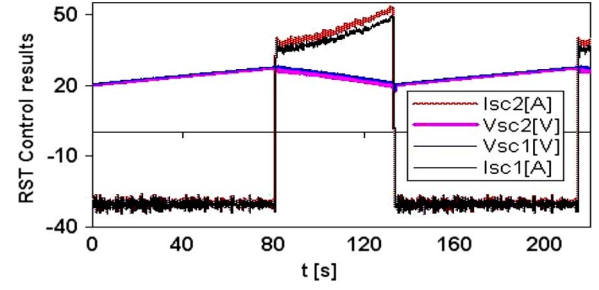


Fig. 18. Voltages and currents of two SCAP modules.

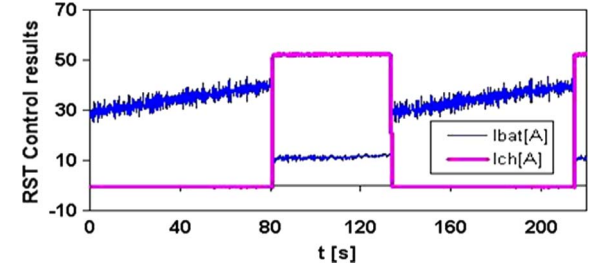


Fig. 19. Battery and active load currents.

at 50 A. The reference currents during the module charge and discharge are $I_{scref} = 60$ A in buck mode and $I_{batref} = 10$ A in boost mode, respectively.

1) *First-Topology Experimental Results:* For this topology, the test bench includes two SCAP modules with ten cells of 2.7 V in series, a battery module of four cells of 12 V in series, two buck-boost converters, two dc-bus voltage filtering capacitors $C_1 = C_2$, two SCAP current smoothing inductances ($L_1 = L_2$), and the battery current smoothing inductance λ . The system is controlled by the microcontroller (PIC18F4431), and the converter topology is shown in Fig. 7. This topology ensures minimum service during a defect in one of the converter or/and SCAP modules. However, it leads to some problems like module balancing when the modules' internal resistances are not identical or when there are unbalanced control times. The SCAP voltages V_{sc1} and V_{sc2} values are identical. The I_{sc1} and I_{sc2} currents are also identical except during the discharge when a light difference appears because of the SCAP module internal resistance dispersion. This difference is due to the connectors. The SCAP module, which disposes the lowest internal resistance, provides the largest current (Fig. 18). During the SCAP discharge (Fig. 19), i.e., between 80 and 135 s, the battery current reference I_{batref} is fixed at 10 A so that, the SCAP modules provide HEV energy request during the transient states via buck-boost converters. The dynamic control results of the dc-bus current I_L and the voltage obtained from these experimental test conditions are shown in Fig. 20. In this case, each converter ensures 20 A, and the remainder current (10 A) is provided by the battery module. These experimental results at a reduced scale show that the proposed energy management strategy is satisfactory, and this strategy can be extrapolated to HEV embedded energy share.

The next paragraph regards power semiconductor (insulated-gate bipolar transistors (IGBTs) and diodes) loss estimation in

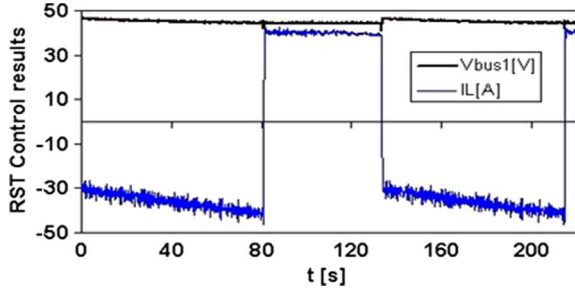


Fig. 20. DC-bus voltage and current.

the traction state of the HEV. The semiconductors present two main types of losses. The first losses are due to semiconductor dynamic resistances (internal), and the second are due to IGBT frequency switching [24], [25]. To illustrate and simplify the IGBT and diode conduction loss estimation, the voltage drops in these components have been considered constant. In this paper, the HEV traction state is considered for the semiconductor loss estimation; in other words, this state supplies the SCAP maximum current (maximum losses).

To estimate these losses, it is necessary to know the boost-converter duty-cycle average values [26]. The first and second boost-converter duty cycles can be estimated using (28). D2 and D4 diode conduction losses resulting from these assumptions can be determined by using (29)

$$\begin{aligned} d_1 &= \frac{V_{bus1} - V_{sc1}}{V_{bus1}} \\ d_2 &= \frac{V_{bus1} - V_{sc2}}{V_{bus1}} \end{aligned} \quad (28)$$

$$\begin{aligned} P_{D2,4} &= (1 - d_{1,2}) \cdot \langle I_{sc1,2} \rangle \cdot V_{(T0)} + R_T \cdot (1 - d_{1,2}) \\ &\quad \cdot \left(1 + \frac{1}{12} \cdot \left(\frac{\Delta I_{sc1,2}}{\langle I_{sc1,2} \rangle} \right)^2 \right) \cdot \langle I_{sc1,2} \rangle^2. \end{aligned} \quad (29)$$

The K_1 and K_3 switch (IGBT) conduction losses can be estimated by using the following:

$$\begin{aligned} P_{K1,3} &= d_{1,2} \cdot \langle I_{sc1,2} \rangle \cdot V_{CE(T0)} + R_{CE} \cdot d_{1,2} \\ &\quad \cdot \left(1 + \frac{1}{12} \cdot \left(\frac{\Delta I_{sc1,2}}{\langle I_{sc1,2} \rangle} \right)^2 \right) \cdot \langle I_{sc1,2} \rangle^2. \end{aligned} \quad (30)$$

The electric power dissipated by all switches during conduction state can be estimated by summing all conduction losses of the diodes and IGBTs

$$P_{cond} = P_{D2} + P_{D4} + P_{K1} + P_{K3}. \quad (31)$$

The switching losses of IGBTs are defined by (32), as shown at the bottom of the page, where f_d , U_{nom} , and I_{nom} are the IGBT switching frequency and the rated voltage and current, re-

TABLE IV
POWER SEMICONDUCTOR PARAMETERS

Symbol	Value	Name
$V_{CE(T0)}$	1.25 V	IGBT threshold voltage
R_{CE}	5.3m Ω	Dynamic resistance of IGBT
$V_{(T0)}$	1.2V	Diodes threshold voltage
R_T	3.5m Ω	Diodes dynamic resistance
ΔI_{sc1}	10% I_{sc1}	I_{sc1} ripple current
ΔI_{sc2}	10% I_{sc2}	I_{sc2} ripple current
$\langle I_{sc1} \rangle, \langle I_{sc2} \rangle$	I_{sc1}, I_{sc2}	Experimental measured currents

spectively. The semiconductor dissipated energies E_{ON_IGBT} , E_{OFF_IGBT} , and E_{OFF_DIODE} corresponding to rated power ($U_{nom} \cdot I_{nom}$) is given in the manufacturer datasheet. Assuming that the SCAP current smoothing inductances are same, the electric power dissipated in the internal resistance ($R_{L1} = R_{L2} = R_L$) of these devices can be determined using

$$\begin{aligned} P_{L12} &= R_L \cdot \left(\left(1 + \frac{1}{12} \cdot \left(\frac{\Delta I_{sc1}}{\langle I_{sc1} \rangle} \right)^2 \right) \cdot \langle I_{sc1} \rangle^2 \right. \\ &\quad \left. + \left(1 + \frac{1}{12} \cdot \left(\frac{\Delta I_{sc2}}{\langle I_{sc2} \rangle} \right)^2 \right) \cdot \langle I_{sc2} \rangle^2 \right). \end{aligned} \quad (33)$$

The dissipated remainder power can be obtained from a difference between the global losses and the aforementioned estimated losses. This difference is presented in following:

$$\begin{aligned} P_{rest} &= (V_{sc1} \cdot I_{sc1} + V_{sc2} \cdot I_{sc2}) - I_L \cdot V_{bus1} \\ &\quad - (P_{L12} + P_{cond} + P_{com}). \end{aligned} \quad (34)$$

The used power semiconductor (SKM400GB124D) parameters extracted from the manufacturer datasheet for the semiconductor loss estimation are summarized in Table IV. The boost-converter efficiency is defined by the ratio between the dc-bus power and SCAP module power as presented in

$$\eta_{p_RST} = \frac{(I_{bus1} + I_{bus2}) \cdot V_{bus1}}{I_{sc1} \cdot V_{sc1} + I_{sc2} \cdot V_{sc2}}. \quad (35)$$

This efficiency depends greatly on SCAP current; in other words, the progressive discharge of the modules is compensated by the SCAP current progressive increase; which ensures that the semiconductor losses increase. The experimental results of the semiconductor (D2, D4, K1, and K3) conduction losses for the two boost converters are shown in Fig. 21, where the P_{K1} and P_{K3} losses increase when the SCAP module voltages decrease. The dissipated power distribution between the power devices corresponding to SCAP maximum current (96 A) is shown in Fig. 22. These losses can be concentrated (Fig. 23) in self-conduction losses (P_{L12}), semiconductor conduction losses (P_{cond}), semiconductor switching losses (P_{com}), and other remainder losses (P_{rest}).

$$\begin{cases} P_{S1,2} = \frac{V_{sc1,2} \cdot I_{sc1,2} \cdot f_d}{U_{nom} \cdot I_{nom}} \cdot (E_{ON_IGBT} + E_{OFF_IGBT} + E_{OFF_DIODE}) \\ P_{com} = P_{S1} + P_{S2} \end{cases} \quad (32)$$

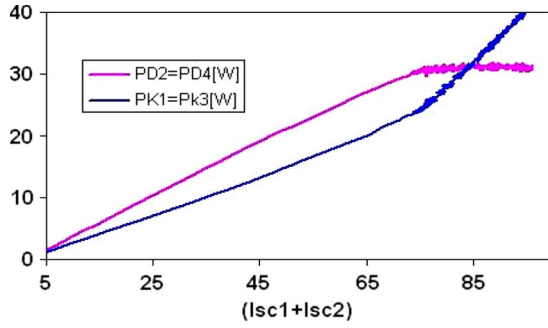


Fig. 21. IGBT (K1, K3) and diode (D2, D4) losses.

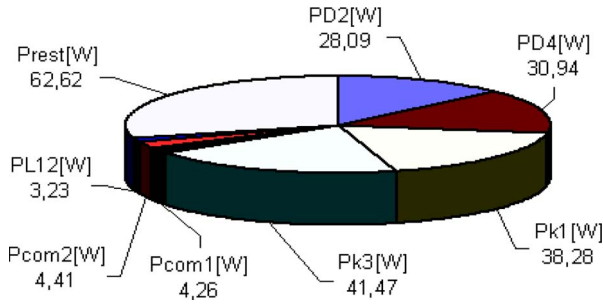
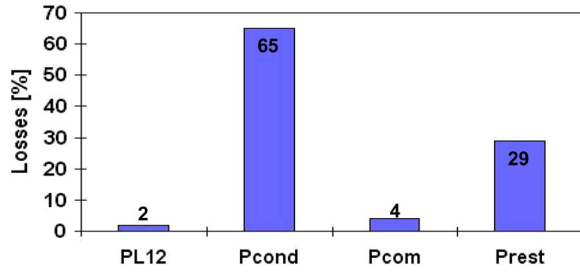
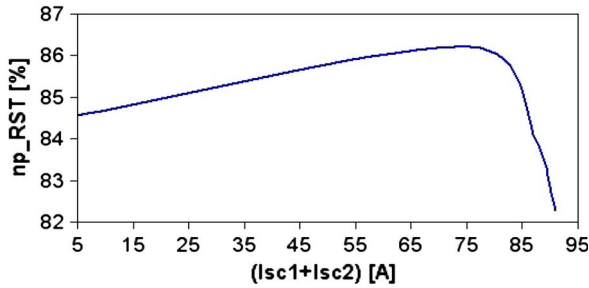
Fig. 22. Power device losses in watts for $I_{sc} = 96$ A.Fig. 23. Power device losses in percent for $I_{sc} = 96$ A.

Fig. 24. First-topology boost-converter efficiency.

The boost-converter experimental efficiency obtained from (35) is shown in Fig. 24. This figure shows that, for $I_{sc} = 80$ A, the boost-converter efficiency is approximately 86%.

However, it is possible to improve this value by optimizing the wiring and using low-loss power semiconductors.

2) *Second-Topology Experimental Results:* To simplify the converter control strategy, the second parallel topology of the buck–boost converters was realized. This test bench also has the same components compared with the first topology. The designed converter topology is shown in Fig. 8, and the

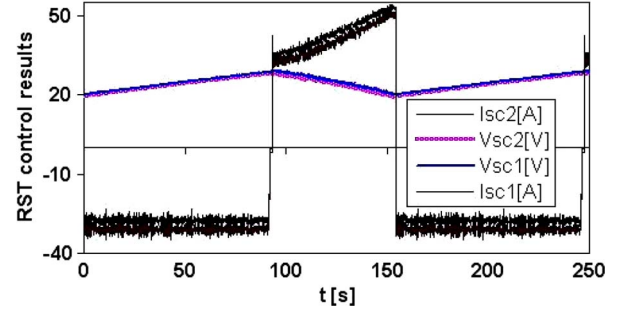


Fig. 25. Voltages and currents of two SCAP modules.

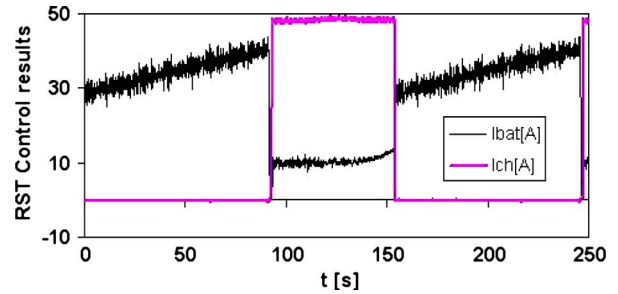


Fig. 26. Battery and active load currents.

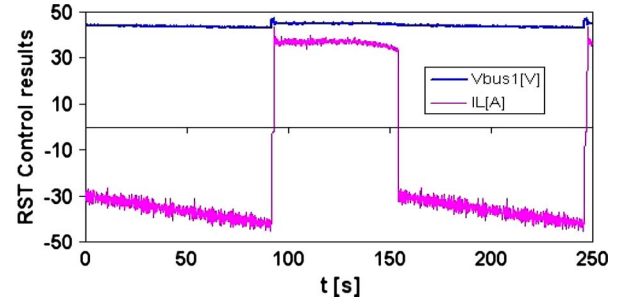


Fig. 27. DC-bus voltage and current.

experimental results of this topology are obtained in similar conditions to that of the first topology.

During the buck-converter mode (Fig. 25), i.e., between 0–91 and 158–246 s, the SCAP reference current $I_{sc1ref} + I_{sc2ref}$ is fixed at 60 A, and the two modules store energy by using a constant current of 30 A for each module.

The difference which appears between I_{sc1} and I_{sc2} currents, shown in Fig. 25, is due to the two buck–boost converter dispersion. This figure shows also the SCAP module corresponding voltages, which are the same.

From 91 to 158 s, the buck–boost converter is in boost mode. In this state, the battery current reference I_{batref} is always fixed at 10 A so that the SCAP modules ensure the HEV energy request. This request (I_{ch}) is always maintained at 50 A, and two SCAP modules ensure the dc-bus current $I_L = 40$ A. Fig. 26 shows that the battery-current-control result is satisfactory and that the hybrid vehicle main power is ensured by SCAP modules via the dc/dc converter. The dc-bus current corresponding to the hybrid vehicle main power is shown in Fig. 27. The boost-converter efficiency estimation for the second topology is similar to that of the first topology, assuming

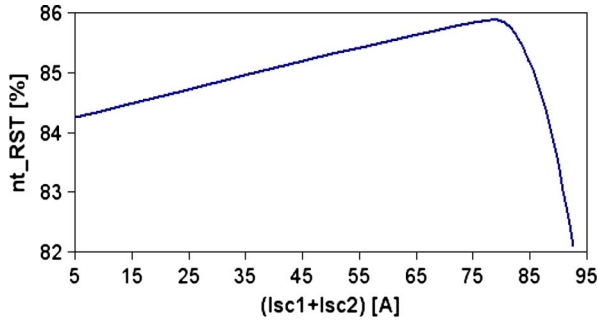


Fig. 28. Second-topology boost-converter efficiency.

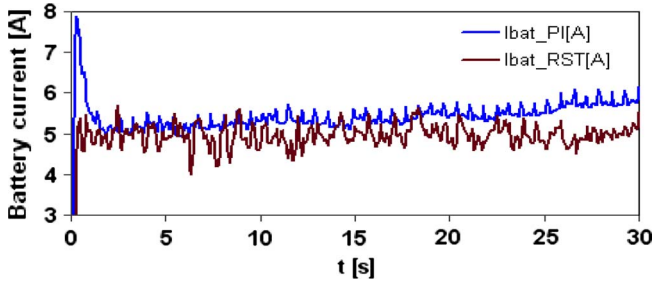


Fig. 29. Battery-current-control results with RST and PI.

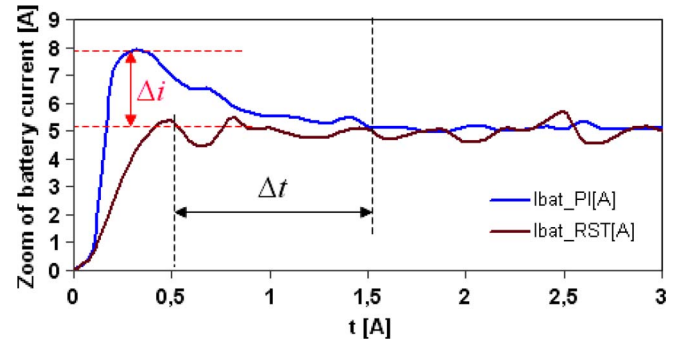


Fig. 30. Zoom of battery-current-control results with RST and PI.

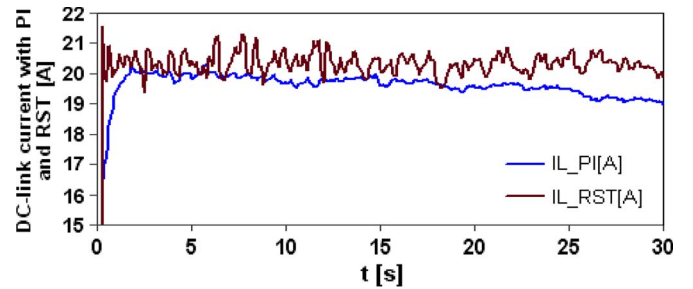


Fig. 31. DC-link (dc-bus) current-control results with RST and PI.

that the SCAP module voltages are the same $V_{sc1} = V_{sc2} = V_{sc}$, which enables one to write

$$n_{t_RST} = \frac{(I_{bus1} + I_{bus2}) \cdot V_{bus1}}{(I_{sc1} + I_{sc2}) \cdot V_{sc}}. \quad (36)$$

The second topology is interesting because of the control simplicity, but the losses caused by the global current are more important than the sum of the losses in the first topology, which explains why the second-topology efficiency (Fig. 28) is weaker than that of first (Fig. 24).

3) Advantages of RST Control Compared with PI: To show the advantages of RST control compared with classical proportional–integral (PI), the experimental tests are carried out by using boost-converter topology (Fig. 8, with $PWM2 = 0$), RST, and PI controllers. These controllers are estimated in identical conditions. In the case of these tests, the battery current reference is $I_{batref} = 5$ A so that the SCAP provides to the HEV the significant power during transient states. To simulate the HEV behavior, a power electronic active load (I_{ch}) is used with a current of 25 A. Fig. 29 shows that the battery current resulting from RST control is more interesting than that of classical PI control, i.e., the PI control result presents a delay $\Delta t = 1$ s compared to RST system, and this difference is shown in Fig. 30. Concerning initial conditions, the polynomial control strategy is also interesting compared with PI as shown in Fig. 30, where $\Delta i = 3$ A, either 60% of I_{batref} . The measured currents on dc link (dc bus) with RST and PI are shown in Fig. 31. These curves show that the polynomial control is more accurate and robust than classical PI.

These experimental results enable one to conclude that the proposed control strategy has better performance (rapid and accurate) compared with PI applied in hybrid vehicle applications.

V. CONCLUSION

The SCAP model presented in this paper is a simplified model based on polynomial capacitance, which describes the SCAP cell energy behavior during the charge and discharge states. In other words, this model does not describe the SCAP behavior before and after the modules charge and discharge.

To avoid one buck–boost converter saturation, the first topology has been proposed for hybrid vehicle energy management. Contrary to this one, the second topology has been proposed for simplifying converter control strategy and decreasing the SCAP current smoothing inductance number. An original strategy of the RST synthesis with polynomial coefficient estimation according to inductances, sampling period, and desired bandwidth has been presented in this paper. This polynomial control strategy is applied to two dc/dc converters for energy management between SCAP and battery. The resulting algorithms are robust and easy to do with a microcontroller or DSP devices.

An experimental study of two dc/dc converter topologies with the polynomial control strategy has been presented. The first topology seems to be more interesting because its efficiency is higher as compared with that of the second topology. The advantages of the polynomial control strategy compared with classical PI techniques applied in HEV applications were highlighted.

REFERENCES

- [1] F. I. Simjee and P. H. Chou, "Efficient charging of supercapacitors for extended lifetime of wireless sensor nodes," *IEEE Trans. Energy Convers.*, vol. 23, no. 3, pp. 1526–1536, May 2008.
- [2] M. Uzunoglu and M. S. Alam, "Modeling and analysis of an FC/UC hybrid vehicular power system using a novel-wavelet-based load sharing algorithm," *IEEE Trans. Energy Convers.*, vol. 23, no. 1, pp. 263–272, Mar. 2008.

- [3] Y. Diab, P. Venet, H. Gualous, and G. Rojat, "Self-discharge characterization and modeling of electrochemical capacitor used for power electronics applications," *IEEE Trans. Power Electron.*, vol. 24, no. 2, pp. 510–517, Feb. 2009.
- [4] S. Barsali and M. Ceraolo, "Dynamical models of lead-acid battery: Implementation issues," *IEEE Trans. Energy Convers.*, vol. 17, no. 1, pp. 16–23, Mar. 2002.
- [5] L. Gao, S. Liu, and R. A. Dougal, "Dynamic lithium-ion battery model for system simulation," *IEEE Trans. Compon. Packag. Technol.*, vol. 25, no. 3, pp. 495–505, Sep. 2002.
- [6] M. Ceraolo, "New dynamical models of lead-acid battery," *IEEE Trans. Power Syst.*, vol. 15, no. 4, pp. 1184–1190, Nov. 2000.
- [7] A. Szumanski and Y. Chang, "Battery management system based on battery nonlinear dynamics modeling," *IEEE Trans. Veh. Technol.*, vol. 57, no. 3, pp. 1425–1432, May 2008.
- [8] B. Schweighofer, K. M. Raab, and G. Brasseur, "Modeling of high power automotive battery by the use of an automated test system," *IEEE Trans. Instrum. Meas.*, vol. 52, no. 4, pp. 1087–1091, Aug. 2003.
- [9] M. B. Camara, H. Gualous, F. Gustin, and A. Berthon, "Control strategy of hybrid sources for transport applications using supercapacitors and battery," in *Proc. IEEE, IPEMC*, Shanghai, China, Aug. 13–16, 2006, vol. 1, pp. 1–5.
- [10] L. Solero, A. Lidozzi, and J. A. Pomilo, "Design of multiple-input power converter for hybrid vehicles," *IEEE Trans. Power Electron.*, vol. 20, no. 5, pp. 1007–1016, Sep. 2005.
- [11] M. B. Camara, H. Gualous, F. Gustin, and A. Berthon, "Design and new control of DC/DC converters to share energy between SCAP and battery in hybrid vehicle," *IEEE Trans. Veh. Technol.*, vol. 57, no. 5, pp. 2721–2735, Sep. 2008.
- [12] J. Moreno, M. E. Ortizar, and J. W. Dixon, "Energy-management system for a hybrid electric vehicle, using ultracapacitors and neural networks," *IEEE Trans. Ind. Electron.*, vol. 53, no. 2, pp. 614–623, Apr. 2006.
- [13] P. Thounthong, S. Rael, and B. Davat, "Control strategy of fuel cell and supercapacitors association for a distributed generation system," *IEEE Trans. Ind. Electron.*, vol. 54, no. 6, pp. 3225–3233, Dec. 2007.
- [14] L. Gao, Z. Jiang, and R. A. Dougal, "Evaluation of active hybrid fuel cell/battery power sources," *IEEE Trans. Aerosp. Electron. Syst.*, vol. 41, no. 1, pp. 346–355, Jan. 2005.
- [15] X. Du, L. Zhou, and H.-M. Tai, "Double-frequency buck converter," *IEEE Trans. Ind. Electron.*, vol. 56, no. 5, pp. 1690–1698, May 2009.
- [16] K. Jin, X. Ruan, M. Yang, and M. Xu, "A hybrid fuel cell power system," *IEEE Trans. Ind. Electron.*, vol. 56, no. 4, pp. 1212–1222, Apr. 2009.
- [17] F. Baalbergen, P. Bauer, and J. A. Ferreira, "Energy storage and power management for typical 4Q-load," *IEEE Trans. Ind. Electron.*, vol. 56, no. 5, pp. 1485–1498, May 2009.
- [18] A. M. Rahimi and A. Emadi, "Active damping in DC/DC power electronic converters: A novel method to overcome the problems of constant power loads," *IEEE Trans. Ind. Electron.*, vol. 56, no. 5, pp. 1428–1439, May 2009.
- [19] S.-Y. Choe, J.-W. Ahn, J.-G. Lee, and S.-H. Baek, "Dynamic simulator for a PEM fuel cell system with a PWM DC/DC converter," *IEEE Trans. Energy Convers.*, vol. 23, no. 2, pp. 669–680, Jun. 2008.
- [20] P. Thounthong, S. Raël, and B. Davat, "Control algorithm of fuel cell and batteries for distributed generation system," *IEEE Trans. Energy Convers.*, vol. 23, no. 1, pp. 148–155, Mar. 2008.
- [21] I. D. Landau, J. Langer, D. Rey, and J. Barnier, "Robust control of a 360° flexible arm using the combined pole placement/sensitivity function shaping method," *IEEE Trans. Control Syst. Technol.*, vol. 4, no. 4, pp. 369–383, Jul. 1996.
- [22] M. B. Camara, D. Fodorien, H. Gualous, D. Bouquain, and A. Miroui, "Hybrid sources control for electric drives traction applications," in *Proc. 19th IEEE Int. Symp. Power Electron., Elect. Drives, Autom. Motion*, Ischia, Italy, Jun. 11–13, 2008, pp. 744–749.
- [23] M. B. Camara, H. Gualous, F. Gustin, and A. Berthon, "Experimental study of buck-boost converters with polynomial control strategy for hybrid vehicles applications," *Int. Rev. Elect. Eng. (IREE)*, vol. 2, no. 4, pp. 601–612, Aug. 2007.
- [24] S. Castagno, R. D. Curry, and E. Loree, "Analysis and comparison of a fast turn-on series IGBT stack and high-voltage-rated commercial IGBTs," *IEEE Trans. Plasma Sci.*, vol. 34, no. 5, pp. 1692–1696, Oct. 2006.
- [25] N. D. Benavides and P. L. Chapman, "Mass-optimal design methodology for DC/DC converters in low-power portable fuel cell applications," *IEEE Trans. Power Electron.*, vol. 23, no. 3, pp. 1545–1555, May 2008.
- [26] M. B. Camara, F. Gustin, H. Gualous, and A. Berthon, "Energy management strategy for coupling supercapacitors and batteries with DC-DC converters for hybrid vehicle applications," in *Proc. 13th IEEE EPE-PEMC*, Poznan, Poland, Sep. 1–3, 2008, pp. 1542–1547.



associate Professor with the Groupe de Recherche en Electrotechnique et Automatique du Havre Laboratory, The University of Le Havre, Le Havre, France.



management.



Mamadou Baïlo Camara was born in Guinea. He received the Dipl.Eng. degree in electrical engineering from the Polytechnic Institute of Conakry (IPC), Conakry, Guinea, in 2003 and the M.S. and Ph.D. degrees from the University of Franche-Comté, Belfort, France, in 2004 and 2007, respectively.

Since 2004, he has been working in power electronics and electric vehicle research projects, involving static converter topologies, supercapacitors, batteries, and electrical energy management for hybrid vehicle applications. He is currently an As-

Hamid Gualous was born in Morocco on January 1967. He received the Ph.D. degree in electronics from the University of Paris XI, Orsay, France, in 1994.

Since 1996, he has been an Associate Professor with the Franche-Comté Electronique Mécanique Thermique et Optique—Sciences et Technologies Institute, University of Franche-Comté, Belfort, France. His main research activities are concerning supercapacitors and fuel cells dedicated to transport applications, power electronics, and energy

Frederic Gustin received the Ph.D. degree from the University of Franche-Comté, Belfort, France, in 2000.

He is currently with the University of Franche-Comté, where his research activities involve power electronics, converters, and simulation methods at the Franche-Comté Electronique Mécanique Thermique et Optique—Sciences et Technologies Institute and where he is currently an Associate Professor with the Institut Universitaire de Technologie de Belfort-Montbéliard.



working in the field of power electronic converters, drives, and electrical power management for electrical vehicles.

Alain Berthon (M'01) received the Dipl. Engineer degree in electrical engineering from the Ecole Nationale Supérieure d'Electricité et de Mécanique, Nancy, France, in 1972 and the Dr. Ing. degree from the University of Franche-Comté, Belfort, France.

He is currently a Professor with the Institut Universitaire de Technologie de Belfort-Montbéliard, University of Franche-Comté, where he is also the Head of the power electronics team at the Franche-Comté Electronique Mécanique Thermique et Optique—Sciences et Technologies Institute. He is



Brayima Dakyo (M'06) received the Dipl. Engineer degree and the Ph.D. degree in engineering from Dakar University, Dakar, Senegal, in 1984 and 1987, respectively, and the Ph.D. degree and Habilitation from The University of Le Havre, Le Havre, France, in 1988 and 1997, respectively.

He is a Full Professor of electrical engineering and the Head of a research team at the Groupe de Recherche en Electrotechnique et Automatique du Havre Laboratory, The University of Le Havre.

His current interests include power electronics, converter-fed electrical machines, electrically powered systems, wind and solar energy systems, and diagnostics.